Ultrafast Nonradiative Decay of a Dipolar Plasmon-like State in Naphthalene

Gowri U. Kuda-Singappulige[a], Andrew Wildman[b], David B. Lingerfelt[b,c], Xiaosong Li[b] & Christine M. Aikens[a,*]

[a]Department of Chemistry, Kansas State University, Manhattan, KS 66506, USA

[b]Department of Chemistry, University of Washington, Seattle, WA 98195, USA

[c]Center for Nanophase Materials Sciences, Oak Ridge National Laboratory, Oak Ridge, TN 37831, USA

[*] cmaikens@ksu.edu, 1-785-532-0954, fax: 1-785-532-6666

Abstract

Motivated by the uncertainty in our understanding of ultrafast plasmon decay mechanisms, we examine the effect of nuclear vibrations on the dynamical behavior of the strong plasmon-like dipole response of naphthalene, known as the β peak. The real-time time dependent density functional (RT-TDDFT) method coupled with Ehrenfest molecular dynamics is used to describe the interconnected nuclear and electronic motion. Several vibrational modes promote drastic plasmon decay in naphthalene. The most astonishing finding of this study is that activation of one particular vibrational mode (corresponding to the B_{1u} representation in D_{2h} point group symmetry) leads to a continuous drop of the dipole response corresponding to the β peak into a totally symmetric, dark, quadrupolar electronic state. A second B_{1u} mode provokes the sharp plasmon-like peak to split due to the breaking of structural symmetry. Nonadiabatic coupling between a B_{2g} vibrational mode and the β peak (a B_{1u} electronic state) gives rise to a B_{3u} vibronic state, which can be identified as one of the p-band peaks that resides close in energy to the β peak energy. Overall, strong nonadiabatic coupling initiates plasmon decay into nearby electronic states in acenes, most importantly into dark states. These findings expand our knowledge about possible plasmon decay processes and pave the way for achieving high optical performance in acene-based materials such as graphene.

Introduction

Interaction of light with subwavelength materials gives rise to a remarkable phenomenon called a plasmon resonance. Upon interacting with incident light at a plasmon resonance frequency, the electrons of plasmonic materials undergo collective oscillations. Because of the potential applications of plasmonic systems in photocatalysis,[1-2] non-linear optics,[2-4] and biomedical applications,[5] etc., plasmonics has become a hot topic in the photonics community. Noble metal nanoparticles comprised of gold and silver can be regarded as the first plasmonic materials ever used, dating back to ancient Rome, although this plasmonicity was not recognized then. To date, many different noble metal nanoparticles of different sizes, shapes and surface environments have been synthesized, each having unique optical properties.[6-9] However, due to the low abundance and high cost of noble metals, alternative materials are of interest, including heavily-doped semiconductor materials as well as 2D materials.[10-12] In particular, due to the strong light confinement effects and tunability of graphene in the terahertz and infrared regions, graphene-based 2D structures have emerged as possible platforms for plasmon-driven devices.[13-18] In addition, recent studies have proposed large enhancements of non-linear properties in graphene.[19-23] However, plasmon loss in graphene severely hampers the performance of optical devices and thus the structural modulation of graphene-based 2D materials to minimize the energy loss is an active research area.[18, 24-25]

The performance of plasmonic devices can be hampered by energy dissipation in plasmonic materials.[26-27] Researchers have proposed that the plasmon can decay via fast formation of hot carriers, electron dephasing, and comparatively slow vibrational dissipation.[28-32] Different pathways may facilitate plasmon decay in different substances. Nevertheless, identifying the most probable non-radiative decay mechanisms in a given type of materials is vital to identify the normal

modes that bring about fast plasmon decay, so that they might be hindered in intelligent device designs.

The purpose of this work is to understand possible mechanisms of fast plasmon dynamics in acenes, the building blocks of graphene, from a theoretical perspective. The low-energy absorption spectra of acenes including naphthalene have been previously reported experimentally[33-34] as well as with different theoretical methods.[35-40] The p-band peaks, the α peak, and the β peak are the main spectral features of acenes. The lowest energy p-band peak and the α peak of naphthalene, also known as ^1L_a and ^1L_b respectively, are observed in the visible region with weak intensities. While the p-band excitations arise due to electron transitions along the short axis of the molecule, the α and β peaks arise from transitions along the long axis. The strong β peak, which is in the UV region, has a plasmon-like character manifested by the constructive nature of the responsible single-particle transitions.[39] Therefore, it is valuable to explore the fast decay processes of this plasmon-like β peak in naphthalene by means of first-principles theories, which can ultimately provide insights into how energy may flow in larger graphene-based plasmonic materials. For example, recent studies demonstrate that electron-phonon coupling plays a key role in intramolecular singlet fission process in low-energy excitations in acenes.[41-45] In this work, we focus on the influence of nuclear motion on the electron dynamics of the strong collective excitation in naphthalene.

In order to describe the ultrafast plasmonic processes accurately, incorporation of a quantum mechanical treatment of electrons is crucial. The well-known linear response theory[46-47] can describe static response properties such as electronic absorption spectra of molecules that result from a weak external field. This method is computationally feasible for calculating low-energy excited states of small metal nanoparticles.[47-54] However, the frequency domain description

of electronic excitations provided by this technique limits its usefulness for our purpose of disentangling the influence of vibrations on the electronic evolution of a system in a superposition of ground and excited states. Real-time electron dynamics methods,[55-57] on the other hand, allow us to access the fluctuation of excited state population in both linear and non-linear regimes and have been developed based on different quantum mechanical approaches such as time-dependent configuration interaction (TD-CI)[58-61] and time-dependent Hartree-Fock/density functional theories (TDHF/TDDFT).[56-57, 62-67] Smith et al.[40] studied the electron dynamics of acenes with a pulsed field at a frequency of 1.55 eV using real-time TDHF method and observed that the lowest energy excited state polarized parallel to the applied field, i.e. the α peak in naphthalene, strongly couples to the field.

Many real-time electron dynamics methods examine only electron movement assuming that the nuclei are stationary. To identify the effect of nuclear motion on the plasmon decay, an ab-initio molecular dynamics (AIMD) method that is capable of accessing excited electronic states should be employed. Most standard AIMD schemes are based on an adiabatic Born-Oppenheimer approximation where the nuclear motion is governed by the ground state electronic potential.[68-71] For our goal of this study however, electronic excited states such as the plasmon-like excitation should be considered, as well as the transitions between excited states, which requires going beyond the adiabatic approximation. Among the current nonadiabatic techniques, the Ehrenfest molecular dynamics scheme serves as the most feasible way to incorporate real-time propagation of excited electrons in an AIMD framework due to its computational tractability relative to other nonadiabatic schemes.[72-73] In this method, the nuclei are treated classically while the electrons are treated quantum mechanically, and the atoms move in a trajectory whose forces are derived from a mean-field potential of the electronic states.[74-76] The mean-field nature of the Ehrenfest dynamics

is ideal for simulating a dense manifold of excited states such as those involved in plasmon-like excitations. This work adopts the Ehrenfest molecular dynamics approach coupled with real-time time dependent density functional theory (RT-TDDFT)[77-78] to investigate the dynamics of the strong β peak of naphthalene upon activation of several vibrational modes to capture possible plasmon decay pathways.

Methodology

We study the effect of vibrational motion on the plasmon dynamics of naphthalene using Ehrenfest molecular dynamics implemented in a development version of the Gaussian software package.[79] Geometry optimizations, frequency calculations, Born-Oppenheimer molecular dynamics (BOMD) and Ehrenfest electron-nuclear dynamics were carried out with the B3LYP[80-82] exchange correlation functional and 6-31G(d,p)[83-87] basis set. The atomic coordinates of the optimized naphthalene are given in Table S1. The transition densities corresponding to excited sates and time dependent difference densities are visualized using Vesta[88] software. The transition densities provide a qualitative picture of the electron density difference in an excited state compared to the density of the ground state.

We follow a similar procedure as in the work of Donati et al.[78] to identify the effect of vibrational motion on the variation of the strong plasmon-like β peak. The electron density is converged in the presence of an electric field perturbation of 0.001 au (~3.57×10^{13} W/cm^2) applied along the longitudinal axis of naphthalene to mimic the activation of the strong β peak excitation. The field is removed after convergence, and the system is propagated using Ehrenfest dynamics where a single normal vibrational mode on the ground electronic state is selectively activated at the beginning of propagation. The initial nuclear velocities were generated randomly, corresponding to an amount of energy equivalent to 5 quanta of the chosen vibrational energy at

the equilibrium geometry. Previous work by Donati et al.[78] showed that plasmon decay in silver nanowires is accelerated with an increased number of vibrational quanta; we thus choose 5 quanta to show the coupling of nuclear and electronic modes within reasonable simulation times in this work. However, our work shows that 5 quanta of energy is in fact a special case for naphthalene which is discussed later in the text.

The current implementation of the Ehrenfest dynamics[74-75] utilizes a triple-step integrator to account for different time scales for the nuclear velocity-Verlet algorithm (Δt_N),[89] nuclear-position coupled midpoint Kohn-Sham integrator (Δt_{Ne}) and RT-TDDFT using modified midpoint and unitary transformation (Δt_e). In this work we use time steps Δt_N = 0.1 fs, Δt_{Ne} = 0.01 fs and Δt_e= 0.001 fs.

Results and Discussion

Optical absorption properties from LR-TDDFT

Figure 1 illustrates the absorption spectrum of naphthalene calculated using LR-TDDFT with the B3LYP/6-31G(d,p) level of theory, highlighting the different types of excitations. The α and β peaks arise at 4.52 eV and 6.10 eV respectively. The three p-band peaks occur at 4.46 eV, 6.26 eV and 8.22 eV. As naphthalene belongs to the D_{2h} point group, the α and β peaks can be assigned to the B_{1u} representation while the p-band peaks can be assigned to the B_{3u} representation according to the cartesian axes of naphthalene shown in Figure 1. Furthermore, it has been previously identified that while the weak α peak arises due to the destructive combination of the two molecular orbital (MO) transitions, HOMO → LUMO + 1 and HOMO – 1 → LUMO, the stronger β peak is a result of constructive addition of the same MO transitions.[38-39] Due to the constructive interference and resulting strong absorption of the β peak, a molecular analog of

plasmonic nature can be identified in naphthalene. The calculated excited state energies and the contributing MO transitions of naphthalene at the equilibrium geometry are tabulated in Table S2.

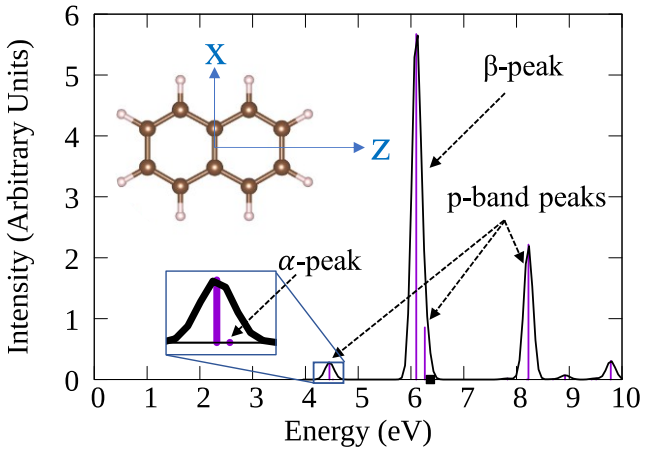

Figure 1. Absorption spectrum of naphthalene calculated from LR-TDDFT (Purple: LR stick spectrum; black: convoluted spectrum using Gaussian curves with Gaussian FWHM = 0.02 eV). Insets show the axes assignments used in the text and a zoomed-in version of part of the spectrum showing the low-intensity α peak. The black square at 6.37 eV indicates a dark electronic state with A_g symmetry.

Effect of vibrational modes on plasmon dynamics

In order to understand the effect of vibrational motion of the molecule on the change of the β band, we activate one vibrational mode with simultaneous excitation of the electronic states polarized along the z axis; the change of the β peak is monitored over time. Vibrational mode energies on the ground electronic state and their D_{2h} point group representations are given in Table S3.

Mode 32 (B_{1u})

The most intriguing vibrational mode which gives rise to a drastic change in the dipole moment over time is normal mode 32 (1407.82 cm^{-1}), which belongs to the B_{1u} representation. First, we compare the dipole response from a BOMD simulation in ground electronic state with

that from an Ehrenfest simulation where the electrons are excited along the long axis of naphthalene (Figure 2a). As shown in Figure 2b, this vibrational mode (and any other mode with B_{1u} representation) is antisymmetric with respect to the reflection through the *xy* plane. Therefore, both electronic and nuclear excitations with B_{1u} symmetry lead the *z*-component of the dipole moment to deviate from 0. Electronic excitation creates a high frequency oscillation centered around the lower frequency oscillation contributed by the nuclear vibration. We examined all of the B_{1u} vibrational modes and observed that the Ehrenfest and BOMD simulations exhibit the same low-frequency nuclear vibrational pattern in all cases (Figure S1). This suggests that electronic perturbation does not noticeably affect the nuclear motion in these simulations.

In the Ehrenfest excited state dynamics with mode 32 activated, we observe a continuous decrement of the dipole strength over the first 600 fs (Figure 2a) and as a consequence, a clean decay of the plasmon-like β peak (Figure 2c). This behavior of the dipole moment demonstrates almost an extinction of the plasmon-like excited state. This leads to the question of where the energy goes over this time scale and whether the system is accessing any "dark" states. Unlike B_{2g} or B_{3g} normal modes, a B_{1u} mode cannot lead to vibronic coupling to another excitation polarized along either *x* or *y* directions. (A discussion of the symmetry considerations for vibronic coupling is provided in the SI). As expected, the variations in the *x*- and *y*-components of the dipole moment do not show a significant increment while the *z*-component of the dipole moment decreases. Our hypothesis is that this B_{1u} normal mode coupling with the B_{1u} electronic excitation leads to energy transfer into a dark electronic state with A_g symmetry that is allowed by vibronic coupling.

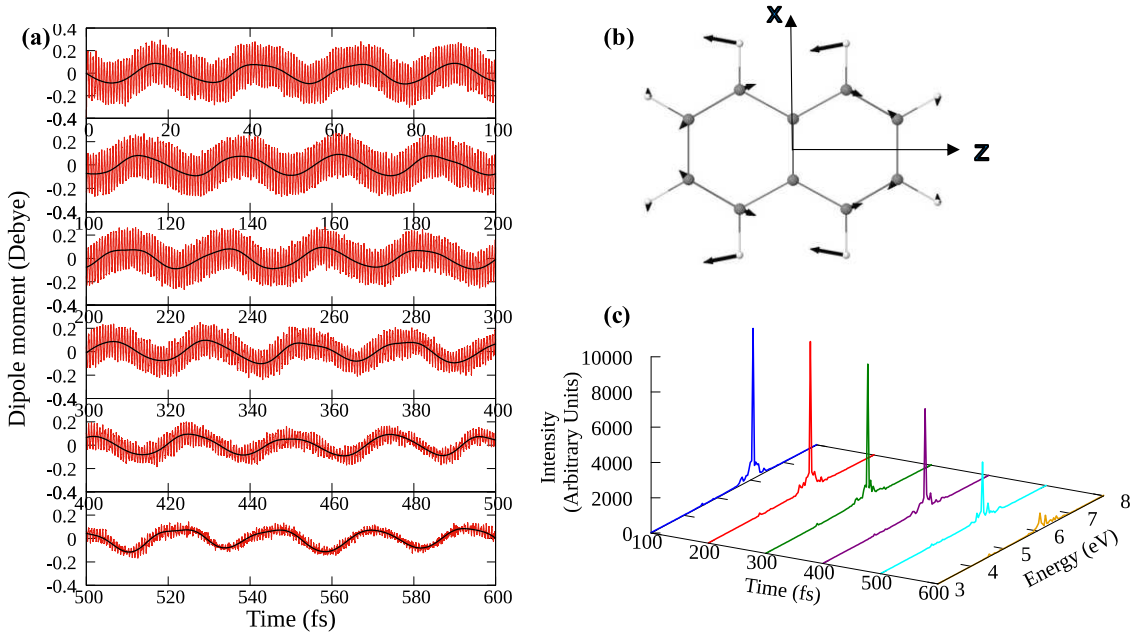

Figure 2. (a) z-component of the dipole moment when mode 32 (B_{1u}) is activated with 5 quanta. Red: Ehrenfest excited state dynamics; Black: ground state BOMD. (b) Vector representation of normal mode 32. (c) Short-time Fourier transforms of 100-fs windows of the z-component of the dipole moment during Ehrenfest dynamics.

However, activation of this totally symmetric dark mode cannot be captured from the dipole response. Instead, the variation of the excited state density compared to the ground state density can be used to answer the question of which states the initial plasmon energy dissipates into. We calculate the difference density $\rho_{m32}^{diff}(t)$ using eq 1 where $\rho'_{m32}(t)$ represents the time dependent electron density during the Ehrenfest dynamics where normal mode 32 is activated and the electric step field is applied, and $\rho^{0}_{m32}(t)$ is the electron density from a similar calculation without an applied electric field. In other words, the difference density reveals how the electron density in the excited state deviates from the ground state in a time-varying situation.

$$\rho_{m32}^{diff}(t) = \rho'_{m32}(t) - \rho^{0}_{m32}(t) \quad (1)$$

The dipole moment variation along the *z* axis over 600 fs is illustrated in Figure 3a and expanded views from 0 to 1 fs and from 580 to 581 fs are shown in Figure 3b and 3c, respectively. The density difference maps calculated using eq 1 at the beginning of the simulation are shown in Figure 3d. The initial difference density at 0 fs can be compared with the transition density corresponding to the β peak excitation shown in Figure 3e, which clearly exhibits the activation of the β peak at the beginning of the Ehrenfest simulation. The positive and negative lobes at the two ends of naphthalene indicate that the electrons have moved from one end to the other compared to the delocalized ground state electron density. The dipole moment variation between positive and negative values clearly displays the electron density sloshing back and forth from one end to the other end of the molecule, in keeping with the traditional picture of a "plasmon-like" excitation. The positive and negative lobes completely change signs from 0 fs to 0.37 fs (Figure 3d). The dipole moment at 0.37 fs is now positive compared to its negative initial value (Figure 3b). Both the dipole moment and the density difference plot return to initial positions near 0.7 fs. Throughout the beginning of the simulation, the time variation of the electron density clearly manifests the character of the plasmon-like electronic excited state (β peak) of the molecule (Figure 2c).

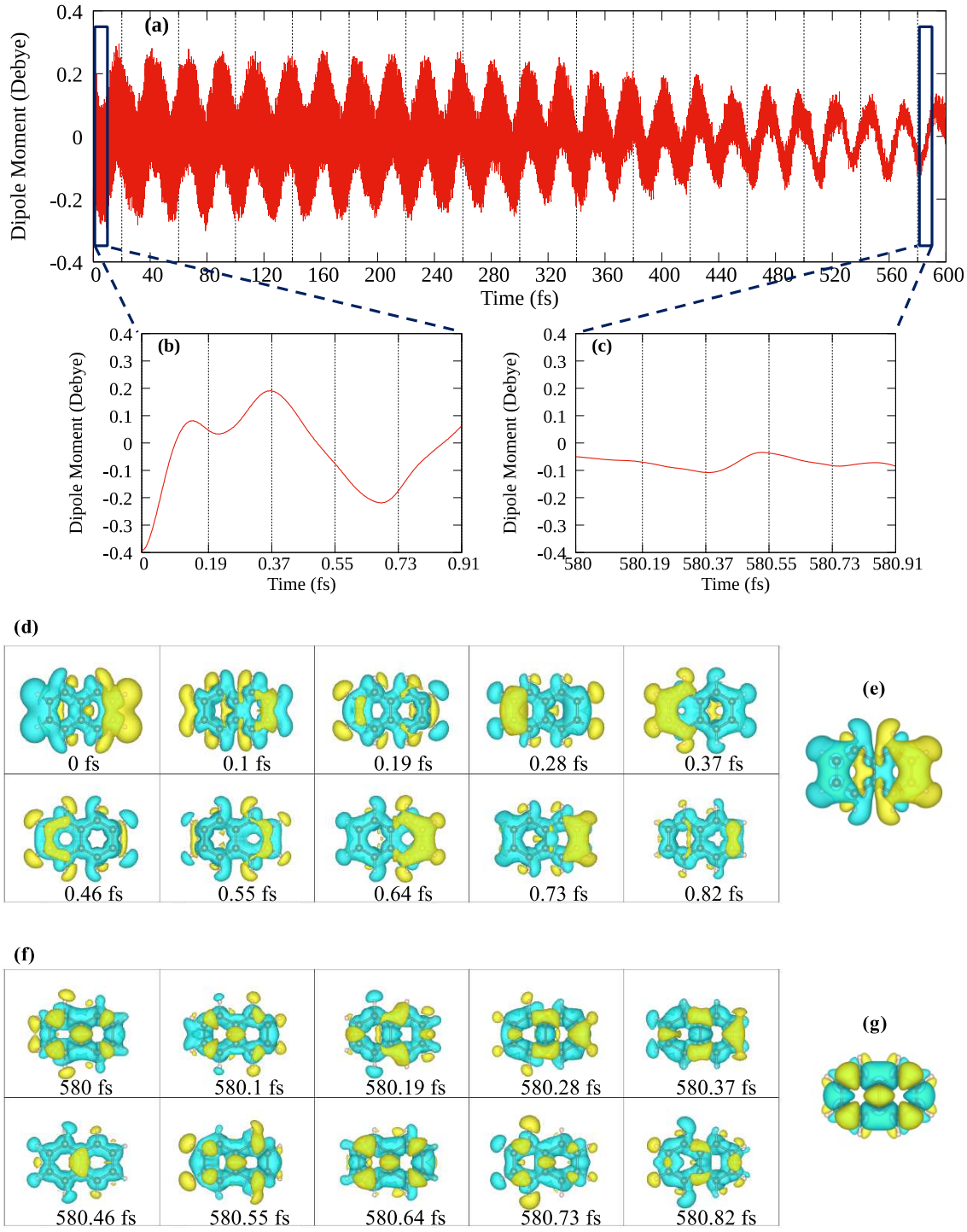

Figure 3. (a) Variation of the *z*-component of the dipole moment for normal mode 32. Detailed dipole moment variation (b) from 0 to 1 fs, (c) from 580 to 581 fs. (d) Variation of the density

difference from 0 fs to 1 fs, (e) transition density of the beta peak (6.10 eV), (f) variation of the density difference from 580 fs to 581 fs and (g) transition density of the 6th excited state (6.37 eV, dark mode). Color code for figures d-g ; yellow: positive; cyan: negative. Isovalues 1×10^{-5} and 5×10^{-4} were used for difference densities (d and f) and transition densities (e and g) respectively.

The strength of the dipole moment decreases gradually from about 300 fs to 600 fs (Figure 3a). To analyze the origin of this behavior, we closely examine the variation of the difference density during 580 fs to 581 fs (Figure 3f), where the dipole moment has lost its strength to a great extent. The density difference no longer has a dipolar character as it did at the initial stages. Instead, the difference density plots throughout this time interval have a quadrupole character. Most importantly, the shape of these difference densities resembles the shape of the transition density corresponding to the 6th excited state (Figure 3g), which is a totally symmetric electronic state (A_g) and hence dipole-forbidden for the D_{2h}-symmetric naphthalene molecule (only electronic transitions from the A_g ground state into B_{1u}, B_{2u}, or B_{3u} excited states are allowed). This dark A_g state has been experimentally identified by Bergman and Jortner[90] using two-photon absorption spectroscopy. Our innovative application of difference densities demonstrates that strong nonadiabatic coupling along this B_{1u} vibrational coordinate can facilitate internal conversion to the dark A_g state. Vibronic selection rules confirm that the direct product of the irreducible representations for the vibrational state (B_{1u}) and the electronic state (B_{1u}) gives rise to a vibronically allowed A_g state (See SI). Above all, the appearance of this dark state correlated with the near-vanishing of the plasmon-like peak clearly illustrates the hitherto-hypothesized mechanism that plasmon decay may occur into nearby dark states.

We extended the simulation with mode 32 until 1200 fs and observed a revival of the β peak after 600 fs. Because the total energy is conserved in the system (i.e. no loss mechanisms are present in a simulation with a single molecule and no bath), we can expect such a revival over time

due to the couplings between the excited states; the system will not be completely trapped in a particular state.

We also examined the dipole response when mode 32 is activated with various numbers of quanta (0-10) during the Ehrenfest dynamics. We observe that only 5 quanta and 10 quanta lead to decay within 600 fs, but not the others (Figure S2). This suggests that the 5 and 10 quanta simulations represent special cases. We initially hypothesized that the energy difference between the β peak (6.10 eV) and the dark state (6.37 eV), i.e. 0.27 eV, might match with the vibrational energy available from 5 vibrational quanta (and 10 quanta) in mode 32. However, the energy available for mode 32 (ν = 0.175 eV) with 5 quanta is calculated to be $(n + 1/2)h\nu$ = 0.960 eV. Further investigations on these energetics are warranted in the future.

The energy conservation during an Ehrenfest molecular dynamics simulation when different quanta of mode 32 are activated is shown in Figure S3. We observe that the quality of energy conservation diminishes over time with increasing number of quanta. (Energy conservation in Ehrenfest dynamics simulations degrades more quickly than in electron-only dynamics with RT-TDDFT.) However, the total energy variation in the 5 quanta case varies only within 5×10^{-5} au (0.00136 eV) during 0-600 fs.

Mode 10 (B_{1u})

Another B_{1u} normal mode that leads to changes in the dipole response over time is mode 10 (634.99 cm^{-1}). Like any other B_{1u} mode, the z-component of the dipole moment exhibits a clear vibrational signature in both BOMD and Ehrenfest dynamics (Figure 4Figure 4a). The vector representation of this B_{1u} normal mode (Figure 4b) displays its antisymmetric nature with respect to the reflection through the xy plane. Note that significant changes in the carbon rings occur in mode 10 (Figure 4b) compared to mode 32 (Figure 2b).

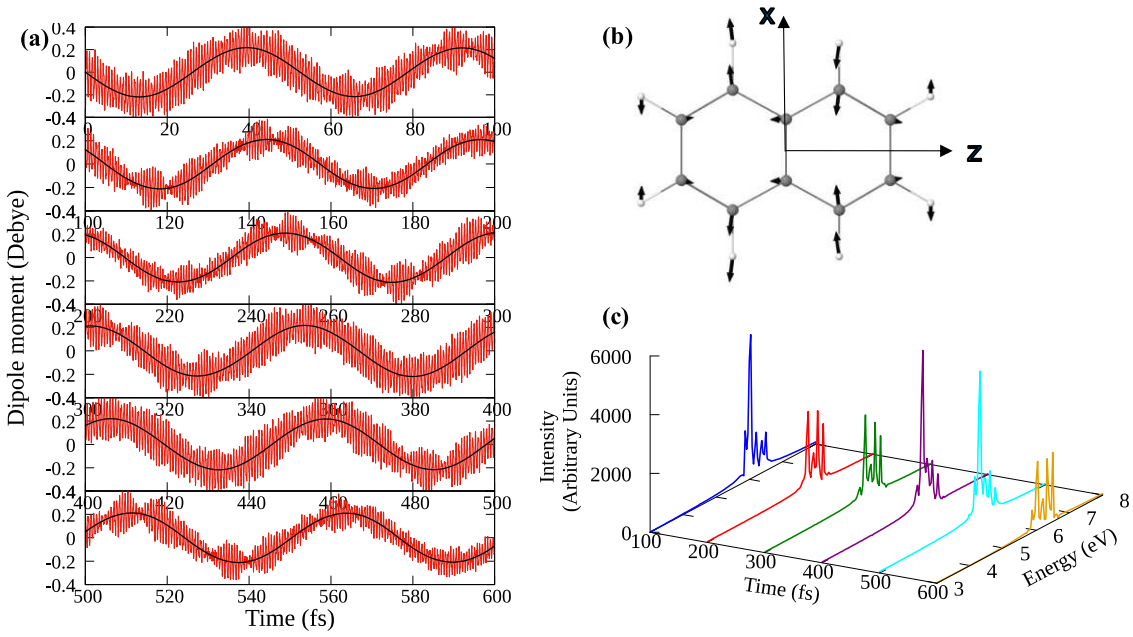

Figure 4. (a) *z*-component of the dipole moment when mode 10 (B_{1u}) is activated with 5 quanta. Red: Ehrenfest excited state dynamics; Black: ground state BOMD. (b) Vector representation of normal mode 10. (c) Short-time Fourier transforms of 100-fs windows of the *z*-component of the dipole moment during Ehrenfest dynamics.

The strength of the dipole moment in this case decreases until about 300 fs and then starts to rise again. This is also illustrated by the short-time Fourier transforms arising from 100 fs windows of the dipole moment given in Figure 4Figure 4c. In addition, a splitting of the plasmonic β peak throughout the simulation is observed. To distinguish the spectral changes due to the structural distortions, we analyze the static LR-TDDFT absorption spectrum of the most distorted geometry of naphthalene when mode 10 is activated, i.e. the geometric structure at 40.0 fs. The distortion of the carbon rings due to the motion of normal mode 10 leads to a splitting of the β peak (Figure 5). The original β peak at the equilibrium geometry (6.10 eV) has shifted to lower energy at 5.96 eV and a new peak appears at 6.46 eV. In addition to the HOMO – 1 → LUMO and HOMO → LUMO + 1 transitions, which are the transitions responsible for the β peak, the two

transitions HOMO – 2 → LUMO + 1 and HOMO – 1 → LUMO + 2 contribute slightly to the peak at 5.96 eV (Table S4). Interestingly, these new transitions appear to be the highest contributors to the peak at 6.46 eV with a slight contribution from HOMO – 1 → LUMO and HOMO → LUMO + 1 transitions. This indicates that lowering of the D_{2h} point group symmetry corresponding to the equilibrium geometry of naphthalene into C_{2v} symmetry at distorted geometries allows new electronic states to emerge. The multiple peaks appearing in the Fourier transforms in Figure 4c are due to the coupling between excited states mediated by the structural distortions. We similarly observe a splitting of the β peak with 0 quanta of energy in mode 10; in this case, a reduction of the dipole strength was not observed (Figure S4).

In conclusion, the B_{1u} normal mode 10 reduces the symmetry of naphthalene which subsequently leads to a splitting of the β peak. In contrast, because mode 32 does not lead to considerable changes in the carbon atom positions, the most distorted structure of mode 32 shows negligible changes in the plasmonic peak. We thus conclude that only the vibrational modes that significantly distort the molecular symmetry tend to split the plasmon-like peak. Nonetheless, normal modes similar to 32 can access electronic states that are optically dark (from the ground state) via ultrafast nonradiative decay from a higher-lying state, as described above.

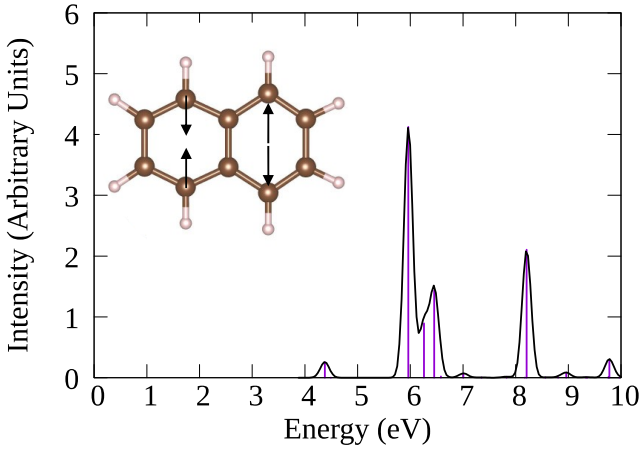

Figure 5. LR-TDDFT absorption spectrum of the geometry of naphthalene at 40.0 fs during the Ehrenfest simulation where the normal mode 10 is activated. The inset shows the geometry of naphthalene at 40.0 fs and the arrows indicate the movement of the carbon atoms compared to the equilibrium geometry.

Modes with B_{2g} symmetry

According to the vibronic coupling selection rules in a D_{2h} molecule, excited B_{2g} vibrational states could couple with excited B_{1u} electronic states (polarized along the z axis) to give rise to B_{3u} vibronic states, which are polarized along the x direction. The variation of the z- and x-components of the dipole moment when mode 35 (1501.48 cm^{-1}, B_{2g}) is activated with 5 quanta along with the excitation of the β peak are shown in Figure 6a (green). The z-component of the dipole moment decreases in magnitude from 0 fs until about 40 fs when it starts to increase again. We observe this decay and growth throughout the 600 fs simulation. Interestingly, at times when the magnitude of the z-component of the dipole moment decreases, the x-component of the dipole moment increases and vice versa, thereby showing the coupling between the dipole moments along the two orthogonal directions. The Fourier transform of the oscillations of the z-component of the dipole moment yields a peak at 6.05 eV (green curve in Figure 6b) which is very close to the β peak energy (pink stick at 6.10 eV in Figure 6b**Error! Reference source not found.**). In

comparison, the Fourier transformed *x*-component of the dipole moment gives rise to two peaks at 6.23 eV and 6.28 eV (blue curve in Figure 6b**Error! Reference source not found.**) which lie near the second p-band excitation energy at 6.26 eV. The slight shifting and the splitting of both green and blue curves are probably due to the interactions between the two electronic states. This phenomenon is even more noticeable when the B_{2g} normal modes in the 1100-1700 cm^{-1} energy range are excited with zero quanta; they exhibit similar coupling of the *z*- and *x*-components of the dipole moment after electronic excitation in the *z*-direction (Figures S5 and S6).

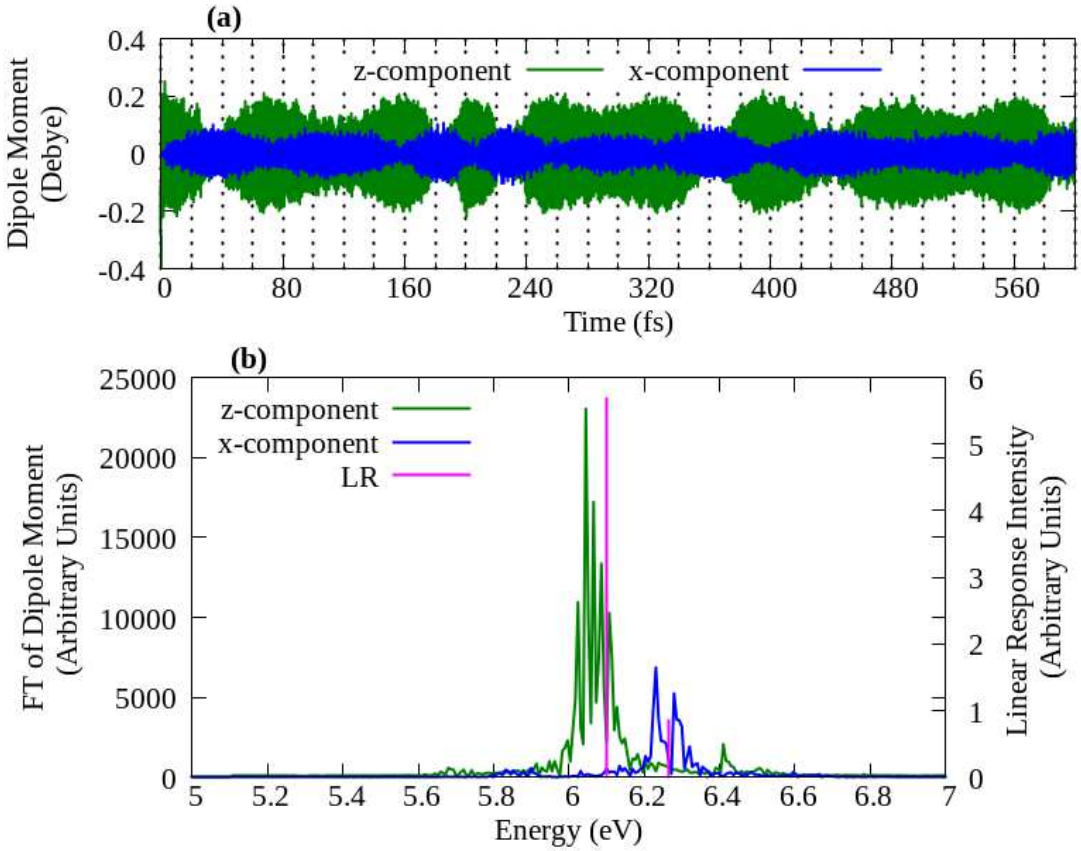

Figure 6. (a) Variation of the dipole moment when mode 35 (B_{2g}) is activated with 5 quanta. (b) Fourier transforms of dipole moment components compared with the LR-TDDFT excitation energy positions. green: *z*-component; blue: *x*-component of the dipole moment; pink: LR-TDDFT stick spectrum.

Summary

The heart of this work is the elucidation of an important plasmon decay pathway, which is activation of dark electronic states mediated by strong nonadiabatic coupling related to certain normal modes. We examined the changes of the strong dipole response of naphthalene when different vibrational modes are activated. The most interesting one, mode 32 (B_{1u}), shows a continuous decrease in the dipole response over 600 fs. Upon activation of this normal mode, a comparison of the excited electron density to the density of the ground state shows that the initial dipolar nature of the electronic oscillation ultimately decays into a quadrupolar form resembling the transition density of the dark electronic excited state that resides close in energy to the bright state. This plasmon decay was found to occur with 5 and 10 quanta of vibrational energy, although not in simulations with other numbers of quanta. It should be noted that 5 quanta of vibrational energy is more than one would expect under normal experimental conditions, but the number of quanta required to access dark states is likely to be system-dependent.

Another interesting nuclear motion that affects the plasmonic peak is normal mode 10 (B_{1u}). This mode largely breaks the symmetry of the molecule compared to the equilibrium geometry, leading to a splitting of the β peak.

The nonadiabatic coupling of B_{2g} normal modes with the B_{1u} plasmon-like β peak, which is polarized along the long axis of naphthalene, initiates energy transfer to the nearest p-band with B_{3u} symmetry, which is polarized along the short axis. Thus, initial excitation polarized in one direction can lead to a dipole response in a different direction.

This work highlights a new understanding of plasmon decay. Nonadiabatic coupling may be one of the dominant pathways of plasmon loss in acenes and potentially in graphene because multiple vibrational modes can couple the plasmon-like state to other excited states as shown in

this work. In addition, fast plasmon decay via nonadiabatic coupling may occur not only in graphene-based plasmonic materials but also in noble metal nanoparticles as governed by the corresponding symmetry rules. This work offers a new route to manipulate the optical properties of plasmonic materials via designing materials with longer (or shorter) plasmon decay lifetimes by adjusting how the vibrational modes couple to the bright and dark electronic excitations.

Supporting Information Available

Optimized coordinates of naphthalene. MO transitions responsible for selected excitations in naphthalene. Energies and symmetry representations of normal modes of naphthalene. Variation of the *z*-component of the dipole moment for B_{1u} normal modes of naphthalene during Ehrenfest dynamics and BOMD in the ground electronic state. Symmetry-adapted selection rules for pure electronic transitions and vibronic transitions. Comparison of dipole moment response and energy conservation during the Ehrenfest simulations when varying numbers of vibrational quanta are added to the system. MO transitions responsible for excitations in the most distorted geometry of naphthalene during activation of normal mode 10. Time and frequency domain *z*- and *x*-components of the dipole moment during an Ehrenfest dynamics with electrons excited along the *z* direction and B_{2g} normal modes of naphthalene activated with zero quanta.

Acknowledgments

This material is based on work supported by the Department of Energy under grant DE-SC0012273. The computing for this project was performed on the Beocat Research Cluster at Kansas State University, which is funded in part by NSF grants CHE-1726332, CNS-1006860, EPS-1006860, and EPS-0919443. The development of the first-principles electronic dynamics is supported by the U.S. Department of Energy (DE-SC0006863 to X.L.). The development of the linear-response TDDFT method for computational spectroscopy was supported by the National Science Foundation (CHE-1856210 to X.L.).

References

1. Hou, W.; Cronin, S. B. A Review of Surface Plasmon Resonance-Enhanced Photocatalysis. *Adv. Funct. Mater.* **2012**, *23*, 1612-1619.

2. Yu, H.; Peng, Y.; Yang, Y.; Li, Z.-Y. Plasmon-Enhanced Light–Matter Interactions and Applications. *Npj Comput. Mater.* **2019**, *5*, 45.

3. Panoiu, N. C.; Sha, W. E. I.; Lei, D. Y.; Li, G. C. Nonlinear Optics in Plasmonic Nanostructures. *J. Opt.* **2018**, *20*, 083001.

4. Genevet, P.; Tetienne, J.-P.; Gatzogiannis, E.; Blanchard, R.; Kats, M. A.; Scully, M. O.; Capasso, F. Large Enhancement of Nonlinear Optical Phenomena by Plasmonic Nanocavity Gratings. *Nano Lett.* **2010**, *10*, 4880-4883.

5. Khlebtsov, N. G.; Dykman, L. A. Optical Properties and Biomedical Applications of Plasmonic Nanoparticles. *J. Quant. Spectrosc. Radiat. Transf.* **2010**, *111*, 1-35.

6. Ogarev, V. A.; Rudoi, V. M.; Dement'eva, O. V. Gold Nanoparticles: Synthesis, Optical Properties, and Application. *Inorg. Mater. Appl. Res.* **2018**, *9*, 134-140.

7. Sardar, R.; Funston, A. M.; Mulvaney, P.; Murray, R. W. Gold Nanoparticles: Past, Present, and Future. *Langmuir* **2009**, *25*, 13840-13851.

8. Fratoddi, I. Hydrophobic and Hydrophilic Au and Ag Nanoparticles. Breakthroughs and Perspectives. *Nanomaterials* **2018**, *8*, 11.

9. Krutyakov, Y. A.; Kudrinskiy, A. A.; Olenin, A. Y.; Lisichkin, G. V. Synthesis and Properties of Silver Nanoparticles: Advances and Prospects. *Russ. Chem. Rev.* **2008**, *77*, 233-257.

10. Naik, G. V.; Shalaev, V. M.; Boltasseva, A. Alternative Plasmonic Materials: Beyond Gold and Silver. *Adv. Mater.* **2013**, *25*, 3264-3294.

11. West, P. R.; Ishii, S.; Naik, G. V.; Emani, N. K.; Shalaev, V. M.; Boltasseva, A. Searching for Better Plasmonic Materials. *Laser Photonics Rev.* **2010**, *4*, 795-808.

12. Li, Y.; Li, Z.; Chi, C.; Shan, H.; Zheng, L.; Fang, Z. Plasmonics of 2D Nanomaterials: Properties and Applications. *Adv. Sci.* **2017**, *4*, 1600430.

13. Ju, L.; Geng, B.; Horng, J.; Girit, C.; Martin, M.; Hao, Z.; Bechtel, H. A.; Liang, X.; Zettl, A.; Shen, Y. R., et al. Graphene Plasmonics for Tunable Terahertz Metamaterials. *Nat. Nanotechnol.* **2011**, *6*, 630-634.

14. Fei, Z.; Rodin, A. S.; Andreev, G. O.; Bao, W.; McLeod, A. S.; Wagner, M.; Zhang, L. M.; Zhao, Z.; Thiemens, M.; Dominguez, G., et al. Gate-Tuning of Graphene Plasmons Revealed by Infrared Nano-Imaging. *Nature* **2012**, *487*, 82-85.

15. Grigorenko, A. N.; Polini, M.; Novoselov, K. S. Graphene Plasmonics. *Nat. Photonics* **2012**, *6*, 749-758.

16. Yan, H.; Li, X.; Chandra, B.; Tulevski, G.; Wu, Y.; Freitag, M.; Zhu, W.; Avouris, P.; Xia, F. Tunable Infrared Plasmonic Devices using Graphene/Insulator Stacks. *Nat. Nanotechnol.* **2012**, *7*, 330-334.

17. Chen, P.-Y.; Argyropoulos, C.; Farhat, M.; Gomez-Diaz, J. S. Flatland Plasmonics and Nanophotonics Based on Graphene and Beyond. *Nanophotonics* **2017**, *6*, 137.

18. Fan, Y.; Shen, N.-H.; Zhang, F.; Zhao, Q.; Wu, H.; Fu, Q.; Wei, Z.; Li, H.; Soukoulis, C. M. Graphene Plasmonics: A Platform for 2D Optics. *Advanced Optical Materials* **2019**, *7*, 1800537.

19. Ren, Q.; You, J. W.; Panoiu, N. C. Large Enhancement of the Effective Second-Order Nonlinearity in Graphene Metasurfaces. *Phys. Rev. B* **2019**, *99*, 205404.

20. Cox, J. D.; García de Abajo, F. J. Nonlinear Graphene Nanoplasmonics. *Acc. Chem. Res.* **2019**, *52*, 2536-2547.

21. You, J. W.; Panoiu, N. C. Plasmon-Induced Nonlinearity Enhancement and Homogenization of Graphene Metasurfaces. *Opt. Lett.* **2019**, *44*, 3030-3033.

22. Jablan, M. Quasiclassical Nonlinear Plasmon Resonance in Graphene. *Phys. Rev. B* **2020**, *101*, 085424.

23. Soavi, G.; Wang, G.; Rostami, H.; Tomadin, A.; Balci, O.; Paradisanos, I.; Pogna, E. A. A.; Cerullo, G.; Lidorikis, E.; Polini, M., et al. Hot Electrons Modulation of Third-Harmonic Generation in Graphene. *ACS Photonics* **2019**, *6*, 2841-2849.

24. Shen, N.-H.; Tassin, P.; Koschny, T.; Soukoulis, C. M. Comparison of Gold- and Graphene-Based Resonant Nanostructures for Terahertz Metamaterials and an Ultrathin Graphene-Based Modulator. *Phys. Rev. B* **2014**, *90*, 115437.

25. Fan, Y.; Shen, N.-H.; Zhang, F.; Zhao, Q.; Wei, Z.; Zhang, P.; Dong, J.; Fu, Q.; Li, H.; Soukoulis, C. M. Photoexcited Graphene Metasurfaces: Significantly Enhanced and Tunable Magnetic Resonances. *ACS Photonics* **2018**, *5*, 1612-1618.

26. Boriskina, S. V.; Cooper, T. A.; Zeng, L.; Ni, G.; Tong, J. K.; Tsurimaki, Y.; Huang, Y.; Meroueh, L.; Mahan, G.; Chen, G. Losses in Plasmonics: From Mitigating Energy dissipation to Embracing Loss-Enabled Functionalities. *Adv. Opt. Photonics* **2017**, *9*, 775-827.

27. Hegde, R. S.; Khatua, S., Chapter 9 - Hot Carrier Generation in Plasmonic Nanostructures: Physics and Device Applications. In *Nanoelectronics*, Kaushik, B. K., Ed. Elsevier: 2019; pp 289-315.

28. Sönnichsen, C.; Franzl, T.; Wilk, T.; von Plessen, G.; Feldmann, J.; Wilson, O.; Mulvaney, P. Drastic Reduction of Plasmon Damping in Gold Nanorods. *Phys. Rev. Lett.* **2002**, *88*, 077402/1-4.

29. Chapkin, K. D.; Bursi, L.; Stec, G. J.; Lauchner, A.; Hogan, N. J.; Cui, Y.; Nordlander, P.; Halas, N. J. Lifetime Dynamics of Plasmons in the Few-Atom Limit. *Proc. Natl. Acad. Sci. U.S.A.* **2018**, *115*, 9134.

30. Lazzarini, C. M.; Tadzio, L.; Fitzgerald, J. M.; Sánchez-Gil, J. A.; Giannini, V. Linear Ultrafast Dynamics of Plasmon and Magnetic Resonances in Nanoparticles. *Phys. Rev. B* **2017**, *96*, 235407/1-11.

31. Liau, Y.-H.; Unterreiner, A. N.; Chang, Q.; Scherer, N. F. Ultrafast Dephasing of Single Nanoparticles Studied by Two-Pulse Second-Order Interferometry. *J. Phys. Chem. B* **2001**, *105*, 2135-2142.

32. Hartland, G. V. Optical Studies of Dynamics in Noble Metal Nanostructures. *Chem. Rev.* **2011**, *111*, 3858-3887.

33. Ligthart, J. A. M.; Karcher, W.; Fordham, R. J.; Dubois, J. J.; Glaude, P. G. J. M. *Spectral Atlas of Polycyclic Aromatic Compounds*; United States: Kluwer Academic Publishers, Norwell, MA, 1985.

34. Birks, J. B.; Christophorou, L. G.; Huebner, R. H. Excited Electronic States of Benzene and Naphthalene. *Nature* **1968**, *217*, 809-812.

35. Coulson, C. A. Excited Electronic Levels in Conjugated Molecules: I. Long Wavelength Ultra-Violet Absorption of Naphthalene, Anthracene and Homologs. *Proc. Phys. Soc.* **1948**, *60*, 257-269.

36. Hashimoto, T.; Nakano, H.; Hirao, K. Theoretical Study of the Valence π→π* Excited States of Polyacenes: Benzene and Naphthalene. *J. Chem. Phys.* **1996**, *104*, 6244-6258.

37. Sony, P.; Shukla, A. Large-Scale Correlated Calculations of Linear Optical Absorption and Low-Lying Excited States of Polyacenes: Pariser-Parr-Pople Hamiltonian. *Phys. Rev. B* **2007**, *75*.

38. Krykunov, M.; Grimme, S.; Ziegler, T. Accurate Theoretical Description of the ^1L_a and ^1L_b Excited States in Acenes Using the All Order Constricted Variational Density Functional Theory Method and the Local Density Approximation. *J. Chem. Theory Comput.* **2012**, *8*, 4434-4440.

39. Guidez, E. B.; Aikens, C. M. Origin and TDDFT Benchmarking of the Plasmon Resonance in Acenes. *J. Phys. Chem. C* **2013**, *117*, 21466-21475.

40. Smith, S. M.; Li, X.; Markevitch, A.; Romanov, D.; Levis, R. J.; Schlegel, H. B. Numerical Simulation of Nonadiabatic Electron Excitation in the Strong-Field Regime. 3. Polyacene Neutrals and Cations. *J. Phys. Chem. A* **2007**, *111*, 6920-6932.

41. Busby, E.; Berkelbach, T. C.; Kumar, B.; Chernikov, A.; Zhong, Y.; Hlaing, H.; Zhu, X. Y.; Heinz, T. F.; Hybertsen, M. S.; Sfeir, M. Y., et al. Multiphonon Relaxation Slows Singlet Fission in Crystalline Hexacene. *J. Am. Chem. Soc.* **2014**, *136*, 10654-10660.

42. Fuemmeler, E. G.; Sanders, S. N.; Pun, A. B.; Kumarasamy, E.; Zeng, T.; Miyata, K.; Steigerwald, M. L.; Zhu, X. Y.; Sfeir, M. Y.; Campos, L. M., et al. A Direct Mechanism of

Ultrafast Intramolecular Singlet Fission in Pentacene Dimers. *ACS Central Science* **2016**, *2*, 316-324.

43. Morrison, A. F.; Herbert, J. M. Evidence for Singlet Fission Driven by Vibronic Coherence in Crystalline Tetracene. *J. Phys. Chem. Lett.* **2017**, *8*, 1442-1448.

44. Deng, G.-H.; Wei, Q.; Han, J.; Qian, Y.; Luo, J.; Harutyunyan, A. R.; Chen, G.; Bian, H.; Chen, H.; Rao, Y. Vibronic Fingerprint of Singlet Fission in Hexacene. *J. Chem. Phys.* **2019**, *151*, 054703.

45. Sanders, S. N.; Kumarasamy, E.; Fallon, K. J.; Sfeir, M. Y.; Campos, L. M. Singlet Fission in a Hexacene Dimer: Energetics Dictate Dynamics. *Chem. Sci.* **2020**, *11*, 1079-1084.

46. Casida, M. E. Time-Dependent Density-Functional Theory for Molecules and Molecular Solids. *Comput. Theor. Chem.* **2009**, *914*, 3-18.

47. Casida, M. E., Time-Dependent Density Functional Response Theory for Molecules. In *Recent Advances in Density Functional Methods*, Chong, D. P., Ed. World Scientific: 1995; Vol. 1, pp 155-192.

48. Aikens, C. M.; Li, S.; Schatz, G. C. From Discrete Electronic States to Plasmons: TDDFT Optical Absorption Properties of Ag_n (n = 10, 20, 35, 56, 84, 120) Tetrahedral Clusters. *J. Phys. Chem. C* **2008**, *112*, 11272-11279.

49. Anak, B.; Bencharif, M.; Rabilloud, F. Time-Dependent density functional study of UV-Visible absorption spectra of small noble metal clusters (Cu_n, Ag_n, Au_n, n = 2–9, 20). *RSC Adv.* **2014**, *4*, 13001-13011.

50. Bae, G.-T.; Aikens, C. M. Time-Dependent Density Functional Theory Studies of Optical Properties of Au Nanoparticles: Octahedra, Truncated Octahedra, and Icosahedra. *J. Phys. Chem. C* **2015**, *119*, 23127-23137.

51. Harb, M.; Rabilloud, F.; Simon, D.; Rydlo, A.; Lecoultre, S.; Conus, F.; Rodrigues, V.; Félix, C. Optical Absorption of Small Silver Clusters: Ag_n, (n=4–22). *J. Chem. Phys.* **2008**, *129*, 194108.

52. Johnson, H. E.; Aikens, C. M. Electronic Structure and TDDFT Optical Absorption Spectra of Silver Nanorods. *J. Phys. Chem. A* **2009**, *113*, 4445-4450.

53. Liao, M.-S.; Bonifassi, P.; Leszczynski, J.; Ray, P. C.; Huang, M.-J.; Watts, J. D. Structure, Bonding, and Linear Optical Properties of a Series of Silver and Gold Nanorod Clusters: DFT/TDDFT Studies. *J. Phys. Chem. A* **2010**, *114*, 12701-12708.

54. Rabilloud, F. Assessment of the Performance of Long-Range-Corrected Density Functionals for Calculating the Absorption Spectra of Silver Clusters. *J. Phys. Chem. A* **2013**, *117*, 4267-4278.

55. Goings, J. J.; Lestrange, P. J.; Li, X. Real-Time Time-Dependent Electronic Structure Theory. *Wiley Interdiscip. Rev. Comput. Mol. Sci.* **2018**, *8*, e1341/1-19.

56. Yabana, K.; Nakatsukasa, T.; Iwata, J. I.; Bertsch, G. F. Real-Time, Real-Space Implementation of the Linear Response Time-Dependent Density-Functional Theory. *Phys. Status Solidi (b)* **2006**, *243*, 1121-1138.

57. Yabana, K.; Bertsch, G. F. Time-Dependent Local-Density Approximation in Real Time. *Phys. Rev. B* **1996**, *54*, 4484-4487.

58. Rohringer, N.; Gordon, A.; Santra, R. Configuration-Interaction-Based Time Dependent Orbital Approach for Ab Initio Treatment of Electronic Dynamics in a Strong Optical Laser Field. *Phys. Rev. A.* **2006**, *74*, 043420.

59. Greenman, L.; Ho, P. J.; Pabst, S.; Kamarchik, E.; Mazziotti, D. A.; Santra, R. Implementation of the Time-Dependent Configuration-Interaction Singles Method for Atomic Strong-Field Processes. *Phys. Rev. A.* **2010**, *82*, 023406.

60. Peng, W.-T.; Fales, B. S.; Levine, B. G. Simulating Electron Dynamics of Complex Molecules with Time-Dependent Complete Active Space Configuration Interaction. *J. Chem. Theory Comput.* **2018**, *14*, 4129-4138.

61. Krause, P.; Klamroth, T.; Saalfrank, P. Time-Dependent Configuration-Interaction Calculations of Laser-Pulse-Driven Many-Electron Dynamics: Controlled Dipole Switching in Lithium Cyanide. *J. Chem. Phys.* **2005**, *123*, 074105.

62. Ding, F.; Van Kuiken, B. E.; Eichinger, B. E.; Li, X. An Efficient Method for Calculating Dynamical Hyperpolarizabilities Using Real-Time Time-Dependent Density Functional Theory. *J. Chem. Phys.* **2013**, *138*, 064104.

63. Lopata, K.; Govind, N. Modeling Fast Electron Dynamics with Real-Time Time-Dependent Density Functional Theory: Application to Small Molecules and Chromophores. *J. Chem. Theory Comput.* **2011**, *7*, 1344-1355.

64. Isborn, C. M.; Li, X. Modeling the Doubly Excited State with Time-Dependent Hartree–Fock and Density Functional Theories. *J. Chem. Phys.* **2008**, *129*, 204107.

65. Baseggio, O.; Fronzoni, G.; Stener, M. A New Time Dependent Density Functional Algorithm for Large Systems and Plasmons in Metal Clusters. *J. Chem. Phys.* **2015**, *143*, 024106/1-12.

66. Castro, A.; Appel, H.; Oliveira, M.; Rozzi, C. A.; Andrade, X.; Lorenzen, F.; Marques, M. A. L.; Gross, E. K. U.; Rubio, A. Octopus: A Tool for the Application of Time-Dependent Density Functional Theory. *Phys. Status Solidi (b)* **2006**, *243*, 2465-2488.

67. Li, X.; Smith, S. M.; Markevitch, A. N.; Romanov, D. A.; Levis, R. J.; Schlegel, H. B. A Time-Dependent Hartree–Fock Approach for Studying the Electronic Optical Response of Molecules in Intense Fields. *Phys. Chem. Chem. Phys.* **2005**, *7*, 233-239.

68. Walker, B. G.; Molteni, C.; Marzari, N. Ab Initio Molecular Dynamics of Metal Surfaces. *J. Phys. Condens. Matter* **2004**, *16*, S2575-S2596.

69. Mark, E. T. Ab Initio Molecular Dynamics: Basic Concepts, Current Trends and Novel Applications. *J. Phys. Condens. Matter* **2002**, *14*, R1297-R1355.

70. Hassanali, A. A.; Cuny, J.; Verdolino, V.; Parrinello, M. Aqueous Solutions: State of the Art in Ab Initio Molecular Dynamics. *Philos. Trans. R. Soc. A* **2014**, *372*, 20120482.

71. Marx, D.; Hutter, J. *Ab Initio Molecular Dynamics: Basic Theory And Advanced Methods*; Cambridge University Press: Cambridge, 2009.

72. Crespo-Otero, R.; Barbatti, M. Recent Advances and Perspectives on Nonadiabatic Mixed Quantum-Classical Dynamics. *Chem. Rev.* **2018**, *118*, 7026-7068.

73. Curchod, B. F. E.; Rothlisberger, U.; Tavernelli, I. Trajectory-Based Nonadiabatic Dynamics with Time-Dependent Density Functional Theory. *ChemPhysChem* **2013**, *14*, 1314-1340.

74. Li, X.; Tully, J. C.; Schlegel, H. B.; Frisch, M. J. Ab Initio Ehrenfest Dynamics. *J. Chem. Phys.* **2005**, *123*, 084106.

75. Ding, F.; Goings, J. J.; Liu, H.; Lingerfelt, D. B.; Li, X. Ab Initio Two-Component Ehrenfest Dynamics. *J. Chem. Phys.* **2015**, *143*, 114105.

76. Wang, F.; Yam, C. Y.; Hu, L.; Chen, G. Time-Dependent Density Functional Theory Based Ehrenfest Dynamics. *J. Chem. Phys.* **2011**, *135*, 044126.

77. Donati, G.; Lingerfelt, D. B.; Petrone, A.; Rega, N.; Li, X. “Watching” Polaron Pair Formation from First-Principles Electron–Nuclear Dynamics. *J. Phys. Chem. A* **2016**, *120*, 7255-7261.

78. Donati, G.; Lingerfelt, D. B.; Aikens, C. M.; Li, X. Molecular Vibration Induced Plasmon Decay. *J. Phys. Chem. C* **2017**, *121*, 15368-15374.

79. Frisch, M. J.; Trucks, G. W.; Schlegel, H. B.; Scuseria, G. E.; Robb, M. A.; Cheeseman, J. R.; Scalmani, G.; Barone, V.; Petersson, G. A.; Nakatsuji, H., et al. *Gaussian Development Version*, Revision J.01+; Gaussian, Inc.: Wallingford CT, 2018.

80. Lee, C.; Yang, W.; Parr, R. G. Development of the Colle-Salvetti Correlation-Energy Formula into a Functional of the Electron Density. *Phys. Rev. B* **1988**, *37*, 785-789.

81. Becke, A. D. A New Mixing of Hartree–Fock and Local Density-Functional Theories. *J. Chem. Phys.* **1993**, *98*, 1372-1377.

82. Stephens, P. J.; Devlin, F. J.; Chabalowski, C. F.; Frisch, M. J. Ab Initio Calculation of Vibrational Absorption and Circular Dichroism Spectra Using Density Functional Force Fields. *J. Phys. Chem.* **1994**, *98*, 11623-11627.

83. Petersson, G. A.; Bennett, A.; Tensfeldt, T. G.; Al-Laham, M. A.; Shirley, W. A.; Mantzaris, J. A Complete Basis Set Model Chemistry. I. The Total Energies of Closed-Shell Atoms and Hydrides of the First-Row Elements. *J. Chem. Phys.* **1988**, *89*, 2193-2218.

84. Francl, M. M.; Pietro, W. J.; Hehre, W. J.; Binkley, J. S.; Gordon, M. S.; DeFrees, D. J.; Pople, J. A. Self-Consistent Molecular Orbital Methods. XXIII. A Polarization-Type Basis Set for Second-Row Elements. *J. Chem. Phys.* **1982**, *77*, 3654-3665.

85. Hariharan, P. C.; Pople, J. A. The Influence of Polarization Functions on Molecular Orbital Hydrogenation Energies. *Theor. Chim. Acta* **1973**, *28*, 213-222.

86. Hehre, W. J.; Ditchfield, R.; Pople, J. A. Self-Consistent Molecular Orbital Methods. XII. Further Extensions of Gaussian-Type Basis Sets for Use in Molecular Orbital Studies of Organic Molecules. *J. Chem. Phys.* **1972**, *56*, 2257-2261.

87. Ditchfield, R.; Hehre, W. J.; Pople, J. A. Self-Consistent Molecular-Orbital Methods. IX. An Extended Gaussian-Type Basis for Molecular-Orbital Studies of Organic Molecules. *J. Chem. Phys.* **1971**, *54*, 724-728.

88. Momma, K.; Izumi, F. *VESTA 3* for Three-Dimensional Visualization of Crystal, Volumetric and Morphology Data. *Journal of Applied Crystallography* **2011**, *44*, 1272-1276.

89. Verlet, L. Computer "Experiments" on Classical Fluids. I. Thermodynamical Properties of Lennard-Jones Molecules. *Physical Review* **1967**, *159*, 98-103.

90. Bergman, A.; Jortner, J. Two-Photon Absorption Spectra of Crystalline Naphthalene and of the Naphthalene Molecule in Solution. *Chem. Phys. Lett.* **1974**, *26*, 323-326.

TOC Graphic

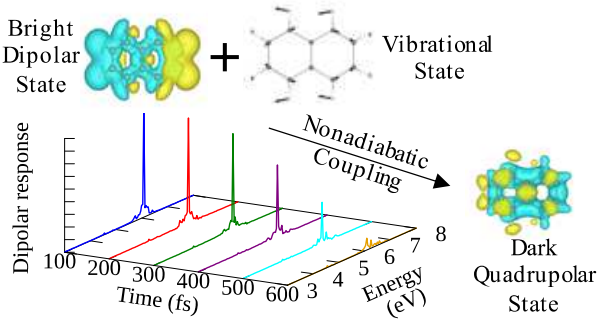
Bright
Dipolar
State
Vibrational
State
Nonadiabatic
Coupling
Dipolar response
100
200
300
400
500
600
Time (fs)
3
4
5
6
7
8
Energy
(eV)
Dark
Quadrupolar
State